

LETTERS

Hidden alternative structures of proline isomerase essential for catalysis

James S. Fraser¹, Michael W. Clarkson², Sheena C. Degnan¹, Renske Erion¹, Dorothee Kern² & Tom Alber¹

A long-standing challenge is to understand at the atomic level how protein dynamics contribute to enzyme catalysis. X-ray crystallography can provide snapshots of conformational substates sampled during enzymatic reactions¹, while NMR relaxation methods reveal the rates of interconversion between substates and the corresponding relative populations^{1,2}. However, these current methods cannot simultaneously reveal the detailed atomic structures of the rare states and rationalize the finding that intrinsic motions in the free enzyme occur on a timescale similar to the catalytic turnover rate. Here we introduce dual strategies of ambient-temperature X-ray crystallographic data collection and automated electron-density sampling to structurally unravel interconverting substates of the human proline isomerase, cyclophilin A (CYPA, also known as PPIA). A conservative mutation outside the active site was designed to stabilize features of the previously hidden minor conformation. This mutation not only inverts the equilibrium between the substates, but also causes large, parallel reductions in the conformational interconversion rates and the catalytic rate. These studies introduce crystallographic approaches to define functional minor protein conformations and, in combination with NMR analysis of the enzyme dynamics in solution, show how collective motions directly contribute to the catalytic power of an enzyme.

It has become widely accepted that not only the chemical steps of an enzymatic reaction, but also protein conformational rearrangements, contribute to the rate acceleration of enzymes^{1,3–6}. For human CYPA, a peptidyl-prolyl *cis/trans* isomerase, NMR relaxation experiments revealed that millisecond motions during catalysis occur in a ‘dynamic network’ that could be described as a two-state interconversion between enzyme conformations bound to the *cis*- and *trans*-Pro substrates. Further, the free enzyme samples the same two conformations on a similar timescale, but with the equilibrium shifted far towards one substate⁴. Although these ‘major’ and ‘minor’ conformations are sampled during turnover, studies aimed at modelling the catalytic mechanism of CYPA^{7–10} have focused on the substrate peptide and have not explained enzyme conformational changes. Moreover, superposition of 48 CYPA crystal structures, including complexes with peptides, inhibitors, and physiological substrates such as the HIV capsid protein^{11,12}, shows no structural heterogeneity that could rationalize the NMR results⁴ (Supplementary Fig. 1).

In search of the catalytically essential, minor conformer of free CYPA detected in solution, we first extended the resolution of the crystal structure to 1.2 Å under cryogenic conditions. This high-resolution structure, however, yielded no evidence for an alternative conformation of the dynamic network. We then used a novel algorithm, Ringer¹³, to systematically sample the electron density around each dihedral angle to discover additional unmodelled side-chain conformers. In a test set of 402 structures determined at 1.5 Å resolution or higher, >15% of the

residues with unbranched side chains have unmodelled secondary electron-density peaks in the range of 0.3–1σ, below the normal noise threshold of 1σ. Strikingly, these peaks are significantly enriched at low-energy rotameric positions, supporting the interpretation that the peaks reflect true minor populations. While Ringer identified discrete side-chain heterogeneity for active-site residues Met 61 and Arg 55 in the 1.2-Å CYPA electron-density map (Supplementary Fig. 2), these alternative conformations were insufficient to explain the extension of the dynamic network away from the active site, particularly to Leu 98 and Ser 99, which showed the largest differences in NMR chemical shifts between the major and minor conformers^{4,14}.

To address this discrepancy between the X-ray and NMR analyses, we collected 1.39-Å diffraction data at ambient temperature to explore the possibility that the low-temperature data collection might alter the conformational distribution in the crystal^{15,16}. Ringer plots indeed uncovered 0.3–1σ features for alternative rotamers of several residues including Leu 98 and Ser 99, in addition to the side-chain heterogeneity observed at cryogenic temperature (Fig. 1a). These results emphasize that crystal freezing can alter conformational distributions.

Modelling the minor conformation of Ser 99 produced a clash of the side-chain hydroxyl group with the Phe 113 ring. Inspection of the electron density surrounding Phe 113 revealed an alternative conformation below the 1σ threshold. $F_o - F_c$ difference density maps calculated without bias from model rebuilding confirmed the alternative conformers of Leu 98, Ser 99 and Phe 113 (Fig. 1b, c, Supplementary Fig. 3). Ringer did not identify the Phe 113 minor rotamer owing to a concomitant shift in the backbone that places Cy within the envelope of the major conformer. This finding emphasizes that no algorithm can yet identify with complete fidelity all structural features without further scrutiny of the electron-density distribution. Refinement verified a network of alternative side-chain rotamers covering the entire active site and extending into the buried regions of the dynamic network previously detected by NMR (Fig. 1d).

The room-temperature diffraction data afford a possible structural rationale for the large NMR chemical-shift differences between the substates in free CYPA. The alternative side-chain rotamers, particularly of Phe 113, are predicted to alter the magnetic environment of the surrounding residues. Only a coupled switch of rotamers is consistent with the steric repulsion of major and minor rotamers, such as the Ser 99/Phe 113 clash in the dynamic network (Fig. 1b).

To critically test the idea that these two conformers interconvert during turnover, we designed a mutation distant from the active site to stabilize the minor CYPA substate. Ser 99, a buried residue in the dynamic network located >14 Å from the catalytic Arg 55, was replaced by Thr to fill the space occupied by both Ser 99 rotamers. This conservative change was designed to stabilize Phe 113 in the ‘out’ position by emulating the steric clash between the minor Ser 99 rotamer and the Phe 113 ‘in’ position. Crystal structures of

¹Department of Molecular and Cell Biology/QB3, University of California, Berkeley, California 94720-3220, USA. ²Department of Biochemistry, Howard Hughes Medical Institute, Brandeis University, Waltham, Massachusetts 02454, USA.

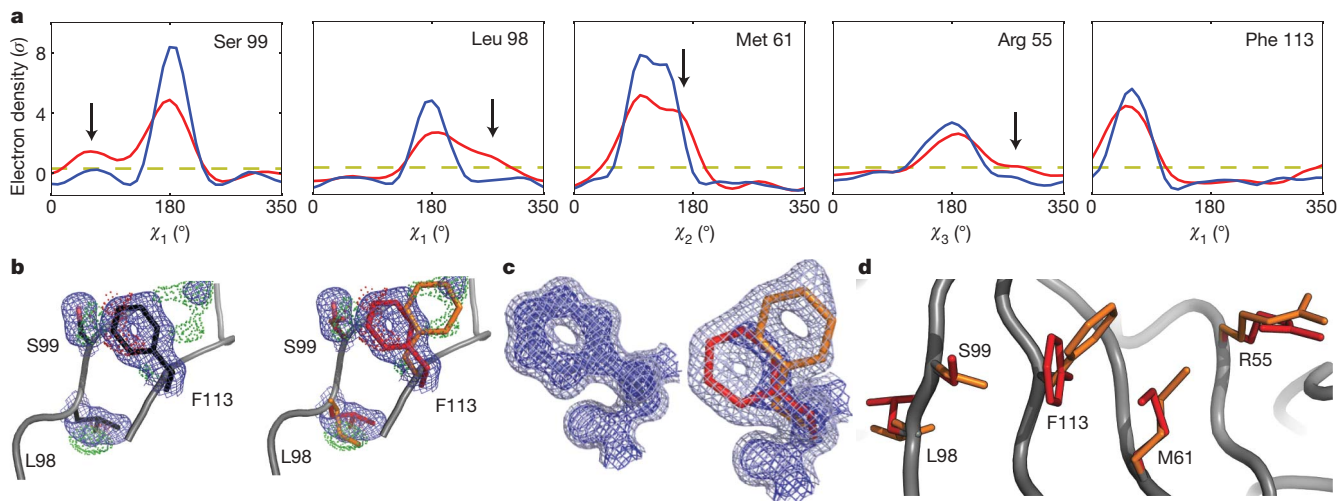


Figure 1 | Room-temperature X-ray crystallography and Ringer analysis detect conformational substates in CYPA. **a**, Local maxima above the 0.3σ threshold (yellow line) in Ringer plots¹³ of electron density by dihedral angle (χ_i) reveal alternative side-chain conformations in room-temperature (red line) but not cryogenic (blue line) electron density for Ser 99, Leu 98, Met 61 and Arg 55. The peak for the minor conformation of Phe 113 occurred within the envelope of the major conformer due to a shift in the protein backbone. **b**, Electron-density maps calculated using room-temperature X-ray data define the alternative conformers of Leu 98, Ser 99 and Phe 113. Shown are $2F_o - F_c$ electron density (blue mesh; 1σ), and positive (green) and negative

(red) $F_o - F_c$ difference density (3σ). **c**, $2F_o - F_c$ composite simulated-annealing omit electron density maps (1.0σ , dark blue; 0.3σ , light blue) show a unique conformation for Phe 113 in the 1.2-Å-resolution cryogenic structure (blue) and distinct major (red) and minor (orange) conformers in the 1.39-Å-resolution room-temperature structure. Electron density around the main chain and the surrounding residues was omitted for clarity. **d**, Steric collisions across the network of major (red) and minor (orange) conformers of Arg 55, Met 61, Phe 113 and Ser 99 explain how side-chain motions link the active site to remote buried residues.

the Ser99Thr mutant, solved at 1.6-Å and 2.3-Å resolution, indeed showed Thr 99 mimicking the alternative Ser 99 conformations, and Phe 113 was detected only in the exposed ‘out’ rotamer (Fig. 2a, b, and Supplementary Fig. 4). This change in rotamer populations was buttressed by three-bond *J*-coupling solution NMR experiments showing that the dominant Phe 113 χ_1 angle changed from +60° in wild-type CYPA to −60° in the Ser99Thr mutant (Supplementary

Table 2). In the Ser99Thr variant structures, Thr 99, Phe 113 and Met 61 occupy the minor rotamers. The positions of Leu 98 and Arg 55 are consistent with either of the rotamers seen in wild-type CYPA. This pattern corroborates the conclusions that Ser 99, Phe 113, Met 61 and possibly Arg 55 are conformationally coupled (Fig. 2c) and that the Ser99Thr mutation severely reduces the population of the major conformation seen in wild-type CYPA.

Connecting this interpretation of the crystal structures to the solution behaviour of the enzyme, NMR detected amide chemical-shift differences between wild-type and Ser99Thr CYPA in most active-site and core residues of the dynamic network (Fig. 3a,b). Although it is tempting to speculate that the Ser99Thr mutation ‘traps’ the minor state of wild-type CYPA based on our crystallographic data (Fig. 2), NMR relaxation-dispersion analysis¹⁷ of the mutant enzyme revealed conformational exchange in both regions that showed collective motions in the wild-type enzyme (Fig. 3c). These regions include residues coupled to the active site (group I) and residues in the 65–85 loops (group II)⁴. In addition, for most of the group I residues, the peaks in Ser99Thr CYPA shift relative to wild type in the same direction as peaks in the previously characterized Lys82Ala variant, which displays a small increase in the population of the minor state⁴. The Ser99Thr mutation, however, causes much larger shifts (Fig. 3b, Supplementary Figs 5, 6), indicating that the populations are inverted. Together with our crystallographic and NMR *J*-coupling data, these results show that the Ser99Thr mutation shifts the structural equilibrium strongly towards a conformation that recapitulates key features of the previously undefined minor state of wild-type CYPA.

In addition to this dramatic population shift, the Ser99Thr mutation also specifically slows the motions of only group I residues by at least two orders of magnitude, pushing them into the slow NMR time regime. The slow dynamics of group I are easily identified by the characteristic increase in dispersion amplitude with increasing temperature, while the fast dynamics in the group II loop region, unaffected by the mutation, are characterized by the opposite trend (Fig. 3d, Supplementary Figs 7,8). This result is reinforced by the static magnetic-field (B_0) dependence of relaxation due to chemical exchange (R_{EX}) as determined by the α value¹⁸: at 25 °C the R_{EX} of group I residues is independent of B_0 ($\langle \alpha \rangle = 0.16$, Supplementary

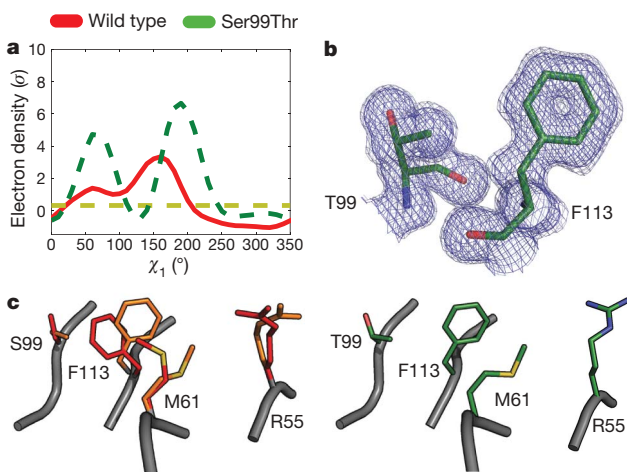


Figure 2 | The structure of the Ser99Thr mutant resembles the minor conformer of wild-type CYPA. **a**, χ_1 Ringer plot (0.3σ threshold is shown as yellow line) of the Ser99Thr mutant (dashed green) and room-temperature, wild-type Ser 99 CYPA structure (red) show that Thr99 occupies both positions populated by the Ser99-OH γ group. The angular offset between the major peaks reflects a backbone shift. **b**, The $2F_o - F_c$ simulated-annealing omit electron density map of the Ser99Thr CYPA mutant (1.0σ , dark blue; 0.3σ , light blue) shows apparently unique conformations for Thr 99 and Phe 113. The structure confirmed the prediction that rotation of Phe 113 to the ‘out’ position is coupled to rotation of the Ser 99 hydroxyl to the minor rotamer. **c**, Phe 113 and Met 61 in Ser99Thr CYPA (green, right) are detected exclusively in the position of the minor state of the wild-type enzyme (orange, left).

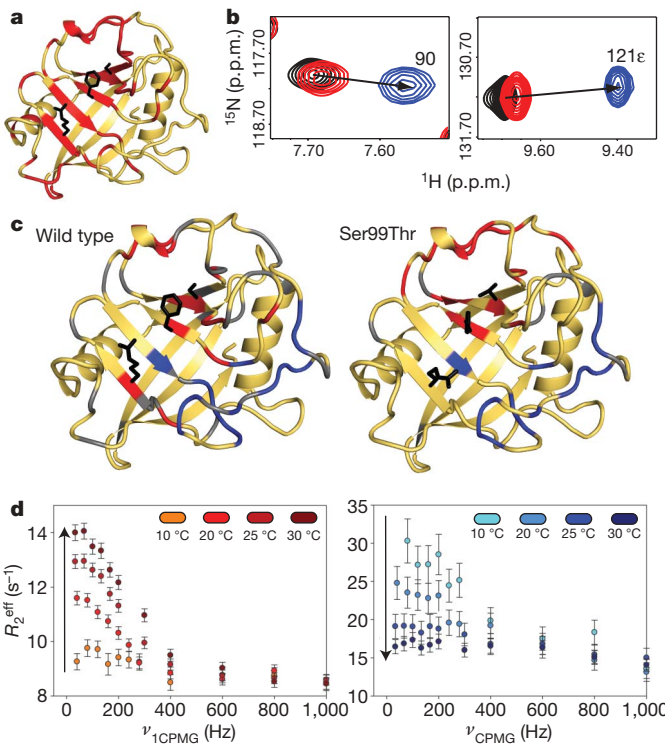


Figure 3 | The Ser99Thr mutation shifts the equilibrium towards the minor wild-type conformation and slows motions in the dynamic network in free CYPA. **a**, Significant ^1H - ^{15}N chemical-shift differences between Ser99Thr and wild-type CYPA (red) propagate through group I residues (Arg 55, Phe 113 and Ser 99 shown as black sticks). **b**, Linear amide chemical shift changes (arrows) between wild-type (black), Lys82Ala (red) and Ser99Thr (blue) CYPA reflect the inversion of the major/minor equilibrium due to the Ser99Thr mutation. **c**, Residues undergoing slow (red) or fast (blue) motions on the NMR timescale in Ser99Thr (right) coincide with previously identified group I (red) and group II (blue) residues in wild-type (left) CYPA (amides in grey are prolines or overlapped peaks). **d**, Temperature dependence of the apparent ^{15}N transverse relaxation rate (R_2^{eff}) at increasing refocusing field strength (ν_{CPMG}) for group I (left) and group II (right) in Ser99Thr CYPA reveal that the mutation impedes group I conformational dynamics ($R_{\text{EX}} \approx k_1$ and R_{EX} increases with temperature). In contrast, group II residues are unaffected by the mutation and display the opposite temperature dependence characteristic of fast motions on the NMR timescale. Dispersion curves were normalized to the intrinsic transverse relaxation rate (R_2^0) at 30 °C. Error bars indicate \pm the root-mean-square deviation of R_2^{eff} calculated from the variance of peak intensities (see Methods).

Table 3), characteristic of slow exchange, while for group II residues the field-dependence is quadratic ($\langle \alpha \rangle = 2.0$), characteristic of fast exchange. Quantitative analysis of the group I residues yields a rate constant of conversion from the major to minor state (k_1) for Ser99Thr CYPA of $1.0 \pm 0.3 \text{ s}^{-1}$ at 10 °C, in contrast to $\sim 60 \text{ s}^{-1}$ for wild-type CYPA⁴. In the slow exchange regime of Ser99Thr, k_1 is well-determined and the major peak represents the true chemical shift of the major state (Fig. 3b).

Given the slower conformational transitions in Ser99Thr CYPA, what is the effect of this mutation on catalytic turnover? In a protease-coupled

enzymatic assay¹⁹, the Ser99Thr mutant showed a 300-fold reduction in the catalytic efficiency of the *cis*-to-*trans* isomerization of the peptide succinyl-AlaAlaProPhe-p-nitroanilide (AAPF) (Fig. 4a). This large reduction in catalytic efficiency resembles the effects of the Arg55Lys mutation, which removes the active-site residue thought to promote the chemical step of the reaction but does not perturb the enzyme dynamics⁴ or global structure (Supplementary Fig. 9). To separate the energetic contributions to the binding and isomerization steps, we measured the dissociation constants of the peptide substrate for the CYPA variants using NMR titration experiments. Peptide affinity (K_D) was weakened

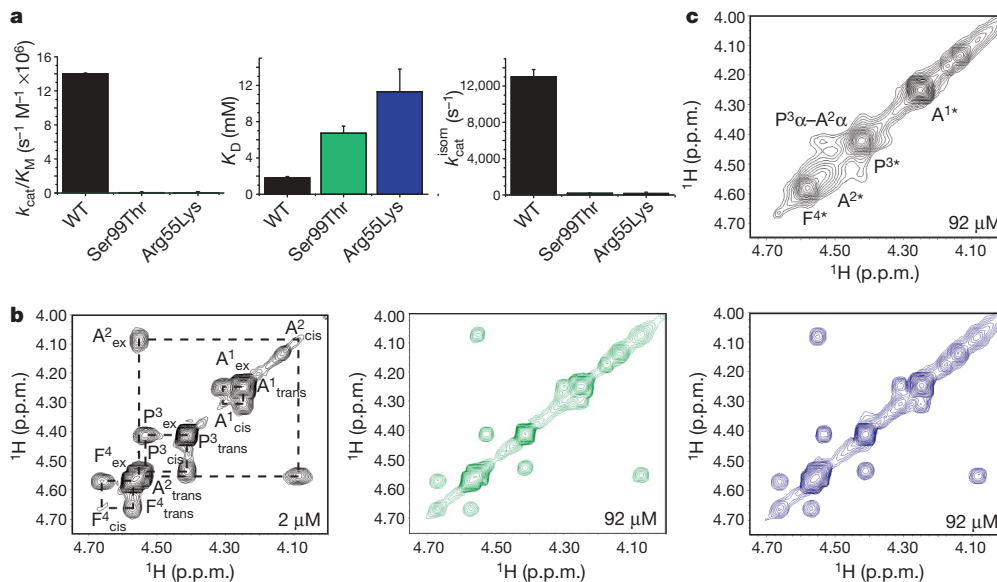


Figure 4 | Impeded motions in the dynamic network severely reduce the catalytic power of a chemically competent enzyme. **a**, Mutations affecting the enzyme dynamics (Ser99Thr) or the chemical step (Arg55Lys) each drastically reduce k_{cat}/K_M (ref. 19) by reducing the bidirectional isomerization step on the enzyme ($k_{\text{cat}}^{\text{isom}}$) and not substrate affinity (K_D) of CYPA. **b**, ^1H - ^1H NOE-exchange spectra at 0.2 s mixing time showing isomerization of the peptide AAPF (1 mM) by catalytic amounts of wild-type (black), Ser99Thr (green) and Arg55Lys (blue) CYPA (concentrations

indicated in the spectra). Assignments and dashed lines connecting exchange (off-diagonal) and auto peaks are included for wild type. Much higher concentrations of the Ser99Thr and Arg55Lys variants are needed relative to wild-type CYPA to obtain similar exchange peaks, reflecting severely reduced catalytic activity. **c**, The *cis*- and *trans*- peaks coalesce (asterisk) for wild-type CYPA at the same enzyme concentration as the mutant forms due to its much greater activity. The only remaining off-diagonal peak is a $\text{P}^3\alpha\text{-A}^2\alpha$ NOE characteristic of a *cis*-prolyl peptide bond.

only 3–6 fold by the Ser99Thr (6.7 ± 0.8 mM) and Arg55Lys (11.3 ± 2.5 mM) mutations (Fig. 4a, Supplementary Fig. 10), suggesting that the major effect of these mutations is on the catalytic turnover number (k_{cat}) and not on the dissociation constant of all enzyme-substrate forms (K_M).

To independently quantify the mutational effects on the rate constant of the isomerization step ($k_{\text{cat}}^{\text{isom}}$), we measured catalysis of the *cis/trans* isomerization directly by ZZ exchange spectroscopy²⁰ (Fig. 4b). These experiments detect the overall rate of converting the entire substrate pool from the *cis*- to the *trans*-Pro conformation and vice versa. The Ser99Thr and Arg55Lys mutations reduce overall turnover by similar amounts compared to wild-type CYPA (Fig. 4, Supplementary Fig. 11). Quantitative fitting of these exchange data²⁰ indicates that the Ser99Thr mutation severely reduces the rate of the bidirectional isomerization step on the enzyme (190 ± 20 s⁻¹ for Ser99Thr compared to $13,000 \pm 800$ s⁻¹ for wild-type CYPA). Strikingly, this reduction (~70-fold) parallels the upper bound for the reduction in the rate constant for the major-to-minor conformational change for group I residues (~60-fold) in the free enzyme (Figs 3c, d).

The similar rate reductions in the free enzyme and of substrate turnover strongly suggest that the slowed fluctuations due to the Ser99Thr mutation underlie the reduction of the catalytic rate. The effects of this ‘molecular traffic-jam’ mutation remote from the active site support the idea that the coupled motions of the dynamic network tied to the rotation of Phe 113 play a key role in turnover. The conformational transition of Phe 113 observed here suggests that the side-chain rotation directly and distinctly impacts *cis*- and *trans*-forms of the proline-substrate during catalysis. Indeed, smaller²¹ or larger⁴ replacements for Phe 113 substantially decrease CYPA activity, suggesting the wild-type enzyme occupies a narrow structural optimum for catalysis. Both the interaction of the Arg 55 side chain with the substrate^{8,9}, which facilitates the chemistry, and side-chain motions throughout the dynamic network, which enable facile interconversion of conformational states, are necessary for catalysis (Fig. 4). Therefore, neither the dynamics nor active-site chemistry that lowers the transition-state energy are sufficient to promote efficient turnover.

Only by collecting X-ray diffraction data at ambient temperature did we observe agreement between the conformational substates detected using NMR and X-ray crystallography. This finding underscores previous studies demonstrating that the conformational distributions in crystals of myoglobin^{22,23} and RNase^{16,24} are restricted at cryogenic temperatures. Unlike these classic studies, which accessed the manifold of crystal structures indirectly through reductions in protein volume, inhibition of ligand binding and reductions in crystallographic *B*-values at cryogenic temperatures, here we use Ringer¹³ to directly sample the electron density. This automated, systematic approach reveals alternative conformational substates. Our results emphasize that the common practices of crystal freezing and building models at the 1σ threshold, rather than capturing the conformational distribution in the crystal, can eliminate information about functionally critical conformations.

Our complementary results from NMR and X-ray crystallography for CYPA demonstrate a general strategy to discover structural ensembles of interconverting substates, to identify which regions of enzymes couple to active sites, and to evaluate the roles of hidden, higher energy conformations in catalysis by other enzymes^{3,25}. Particularly by identifying structurally remote residues that couple to the active site, defining the multiple conformations that contribute to function can afford a deeper understanding of the effects of sequence variation in disease and evolution²⁶. Such knowledge may enable progress not only in understanding and manipulating the mechanisms of numerous macromolecular systems, but also in defining the manifold of conformations accessible to inhibitors and therapeutics²⁷.

METHODS SUMMARY

CYPA was purified as described⁴. Crystals were grown at pH 7.5 using PEG3350 or DL-malate as precipitants. All X-ray data sets derive from single crystals. For room-temperature data collection, we used the Rigaku free mounting device at ALS Beamline 12.3.1²⁸. Short exposures and crystal translation every 10 frames limited radiation damage. Ringer analysis was performed by real-space sampling of electron density around side-chain dihedral angles¹³. Inspection of plots of electron density versus dihedral angle revealed Ringer peaks above 0.3σ that guided placement of alternative conformers. This modelling process was performed iteratively using both conventional and simulated-annealing composite omit maps.

Constant-time ¹⁵N backbone CPMG TROSY relaxation-dispersion data¹⁷ were collected in an interleaved manner on Varian INOVA 500 and 600 spectrometers and a Bruker AVANCE-800 equipped with a cryoprobe. Dispersion curves were fitted to the full Carver-Richards equation²⁹, confirming the results for wild-type CYPA where the exchange is in the intermediate to fast time regime⁴. In contrast, for Ser99Thr CYPA, global fits of dispersion of group-I residues at all temperatures, assuming temperature-independent $\Delta\omega$, unambiguously revealed exchange in the slow regime ($R_{\text{EX}} \approx k_1$, rate constant for efflux from the major state). Numerical fitting and estimation of the dispersion amplitude gave the same rate constant k_1 at 10 °C within experimental error.

Three-bond, aromatic *J* couplings were obtained at 25 °C as described³⁰. Dissociation constants for AAPF were obtained by titrating the peptide into a solution of 0.2 mM CYPA at 6 °C and fitting the resulting chemical shifts to single-site exchange. The enzyme-catalysed *cis/trans* isomerization rates at 6 °C were measured using ¹H-¹H NOESY spectra of AAPF and fitting the data to equations for ZZ exchange²⁰. The bidirectional $k_{\text{cat}}^{\text{isom}}$ was calculated from the fitted exchange rate using the K_D measured in titrations (see Online Methods).

Full Methods and any associated references are available in the online version of the paper at www.nature.com/nature.

Received 13 August; accepted 26 October 2009.

1. Henzler-Wildman, K. & Kern, D. Dynamic personalities of proteins. *Nature* **450**, 964–972 (2007).
2. Mittermaier, A. & Kay, L. E. Review—new tools provide new insights in NMR studies of protein dynamics. *Science* **312**, 224–228 (2006).
3. Boehr, D. D., McElheny, D., Dyson, H. J. & Wright, P. E. The dynamic energy landscape of dihydrofolate reductase catalysis. *Science* **313**, 1638–1642 (2006).
4. Eisenmesser, E. Z. et al. Intrinsic dynamics of an enzyme underlies catalysis. *Nature* **438**, 117–121 (2005).
5. Hammes-Schiffer, S. & Benkovic, S. J. Relating protein motion to catalysis. *Annu. Rev. Biochem.* **75**, 519–541 (2006).
6. Schramm, V. L. & Shi, W. Atomic motion in enzymatic reaction coordinates. *Curr. Opin. Struct. Biol.* **11**, 657–665 (2001).
7. Agarwal, P. K. *Cis/trans* isomerization in HIV-1 capsid protein catalyzed by cyclophilin A: insights from computational and theoretical studies. *Proteins* **56**, 449–463 (2004).
8. Hamelberg, D. & McCammon, A. Mechanistic insight into the role of transition-state stabilization in cyclophilin A. *J. Am. Chem. Soc.* **131**, 147–152 (2009).
9. Li, G. H. & Cui, Q. What is so special about Arg 55 in the catalysis of cyclophilin A? Insights from hybrid QM/MM simulations. *J. Am. Chem. Soc.* **125**, 15028–15038 (2003).
10. Trzesniak, D. & Van Gunsteren, W. F. Catalytic mechanism of cyclophilin as observed in molecular dynamics simulations: pathway prediction and reconciliation of X-ray crystallographic and NMR solution data. *Protein Sci.* **15**, 2544–2551 (2006).
11. Howard, B. R., Vajdos, F. F., Li, S., Sundquist, W. I. & Hill, C. P. Structural insights into the catalytic mechanism of cyclophilin A. *Nature Struct. Biol.* **10**, 475–481 (2003).
12. Ke, H. M. & Huai, Q. Crystal structures of cyclophilin and its partners. *Front. Biosci.* **9**, 2285–2296 (2004).
13. Lang, P. T. et al. Automated electron-density sampling reveals widespread conformational polymorphism in proteins. *Protein Sci.* (submitted).
14. Eisenmesser, E. Z., Bosco, D. A., Akke, M. & Kern, D. Enzyme dynamics during catalysis. *Science* **295**, 1520–1523 (2002).
15. Halle, B. Biomolecular cryocrystallography: structural changes during flash-cooling. *Proc. Natl. Acad. Sci. USA* **101**, 4793–4798 (2004).
16. Rasmussen, B. F., Stock, A. M., Ringe, D. & Petsko, G. A. Crystalline ribonuclease A loses function below the dynamical transition at 220 K. *Nature* **357**, 423–424 (1992).
17. Loria, J. P., Rance, M. & Palmer, A. G. A TROSY CPMG sequence for characterizing chemical exchange in large proteins. *J. Biomol. NMR* **15**, 151–155 (1999).
18. Millet, O., Loria, J. P., Kroenke, C. D., Pons, M. & Palmer, A. G. The static magnetic field dependence of chemical exchange linebroadening defines the NMR chemical shift time scale. *J. Am. Chem. Soc.* **122**, 2867–2877 (2000).

19. Kofron, J. L., Kuzmic, P., Kishore, V., Colonbonilla, E. & Rich, D. H. Determination of kinetic constants for peptidyl prolyl *cis-trans* isomerases by an improved spectrophotometric assay. *Biochemistry* **30**, 6127–6134 (1991).
20. Farrow, N. A., Zhang, O. W., Forman-Kay, J. D. & Kay, L. E. A heteronuclear correlation experiment for simultaneous determination of ^{15}N longitudinal decay and chemical exchange rates of systems in slow equilibrium. *J. Biomol. NMR* **4**, 727–734 (1994).
21. Zydowsky, L. D. *et al.* Active site mutants of human cyclophilin A separate peptidyl-prolyl isomerase activity from cyclosporine A binding and calcineurin inhibition. *Protein Sci.* **1**, 1092–1099 (1992).
22. Frauenfelder, H. *et al.* Thermal expansion of a protein. *Biochemistry* **26**, 254–261 (1987).
23. Frauenfelder, H., Petsko, G. A. & Tsernoglou, D. Temperature-dependent X-ray diffraction as a probe of protein structural dynamics. *Nature* **280**, 558–563 (1979).
24. Tilton, R. F., Dewan, J. C. & Petsko, G. A. Effects of temperature on protein structure and dynamics: X-ray crystallographic studies of the protein ribonuclease-A at nine different temperatures from 98 to 320K. *Biochemistry* **31**, 2469–2481 (1992).
25. Beach, H., Cole, R., Gill, M. L. & Loria, J. P. Conservation of μs -ms enzyme motions in the apo- and substrate-mimicked state. *J. Am. Chem. Soc.* **127**, 9167–9176 (2005).
26. Tokuriki, N. & Tawfik, D. S. Protein dynamism and evolvability. *Science* **324**, 203–207 (2009).
27. Lee, G. M. & Craik, C. S. Trapping moving targets with small molecules. *Science* **324**, 213–215 (2009).
28. Kiefersauer, R. *et al.* A novel free-mounting system for protein crystals: transformation and improvement of diffraction power by accurately controlled humidity changes. *J. Appl. Crystallogr.* **33**, 1223–1230 (2000).
29. Davis, D. G., Perlman, M. E. & London, R. E. Direct measurements of the dissociation-rate constant for inhibitor-enzyme complexes via the T_{1p} and T_2 (CPMG) methods. *J. Magn. Reson. Ser. B* **104**, 266–275 (1994).
30. Hu, J. S., Grzesiek, S. & Bax, A. Two-dimensional NMR methods for determining χ_1 angles of aromatic residues in proteins from three-bond $J_{\text{CC}\gamma}$ and $J_{\text{NC}\gamma}$ couplings. *J. Am. Chem. Soc.* **119**, 1803–1804 (1997).

Supplementary Information is linked to the online version of the paper at www.nature.com/nature.

Acknowledgements We thank S. Marqusee and B. Krantz for discussions; S. Classen, G. Meigs, J. Holton, A. Samelson, N. Echols, P. Afonine, and the Phenix team for technical support; J. Tainer for access to Rigaku free-mounting device at ALS Beamline 12.3.1; J. Pelton and D. Wemmer for providing essential help and access to NMR facilities. J.S.F. was supported by US NSF and Canadian NSERC fellowships. This work was funded by the US National Institutes of Health (to T.A.) and the US National Institutes of Health, the US Department of Energy Office of Basic Energy Sciences, and the Howard Hughes Medical Institute (to D.K.).

Author Contributions J.S.F., S.C.D. and R.E. performed the X-ray experiments, M.W.C. performed the NMR experiments, and M.W.C. and J.S.F. performed the activity and binding assays. J.S.F., M.W.C., D.K. and T.A. analysed data and wrote the paper. All authors contributed to data interpretation and commented on the manuscript.

Author Information Atomic coordinates and structure factors for the reported crystal structures have been deposited in the PDB under accession codes 3KOM, 3KON, 3KOO, 3KOP, 3KOQ and 3KOR. Reprints and permissions information is available at www.nature.com/reprints. Correspondence and requests for materials should be addressed to T.A. (tom@ucxray.berkeley.edu) or D.K. (dkern@brandeis.edu).

METHODS

Crystallography. The standard purification⁴ was augmented with a Superdex S75 column (GE Healthcare) equilibrated in 20 mM HEPES pH 7.5, 100 mM NaCl and 0.5 mM TCEP. Crystals (wild-type and Ser99Thr) with P2₁2₁ symmetry were grown by hanging-drop vapour diffusion by mixing an equal volume of well solution (100 mM HEPES pH 7.5, 22% PEG 3350, 5 mM TCEP) and protein (wild-type CYPA at 60 mg ml⁻¹ and mutants at 40 mg ml⁻¹). Trigonal (P3₁21) crystals of Ser99Thr and Arg55Lys CYPA were grown similarly from 1.8 M DL-malic acid. For cryogenic data sets (collected at 100 K), crystals were flash frozen in liquid nitrogen with well solution plus 15% xylitol as a cryoprotectant for the orthorhombic crystals and 10% glycerol for the trigonal crystals. Wild-type CYPA cryogenic X-ray data were collected at Beamline 9-1 at the Stanford Synchrotron Radiation Laboratory. Ser99Thr and Arg55Lys cryogenic data sets were collected at Beamline 8.3.1 at the Lawrence Berkeley National Laboratory Advanced Light Source (ALS).

Room-temperature X-ray data were collected at 15 °C with 96% humidity using a temperature- and humidity-controlled goniometer head²⁸ (the Rigaku free-mounting device) at ALS Beamline 12.3.1. To limit the effects of radiation damage while maintaining high signal-to-noise, we collected short exposures (0.1 s) for 180° with 1° oscillations. A large crystal (1 mm × 0.5 mm × 0.3 mm) was translated halfway through this rapid collection protocol. Following this initial low-exposure pass, an additional complete data set of 90° with longer exposures (1 s) was collected while translating the crystal every 10 frames. During data processing, we ensured that radiation damage had not degraded the data quality by subdividing the data into subsets of 45 frames and confirming that unit cell parameters, scale factors and χ^2 statistics were consistent throughout the data set³¹. Owing to the short total exposure time (108 s), the limited exposure of each spot on the crystal, the size of the crystal and the finite rate of crystal damage, the data were not significantly influenced by radiation damage.

Reflections were processed using HKL2000³². Structures were solved using PHASER³³ through phenix.automr³⁴ with 2CPL chain A as the search model. To corroborate the features of residues 98, 99 and 113 observed in the initial electron density, reflections were processed using MOSFLM, through ELVES³⁵, and XDS, through XIA2³⁶, and the structures were additionally solved using 1RMH chain A as the search model. The features described in the text were consistent across electron-density maps calculated from data processed with all three programs and both molecular-replacement search models.

Coordinates, atomic displacement parameters, and occupancy (where appropriate) were refined using phenix.refine³⁴ with manual rebuilding using COOT³⁷. Validation was performed using MOLPROBITY³⁸ and PROCHECK³⁹. Data collection, processing, refinement, and validation statistics are listed in Supplementary Table 1. Structural figures were prepared using PyMol⁴⁰.

Ringer. Ringer¹³ analyses electron density in real space around the dihedral angles of the modelled side chains to discover unmodelled alternative conformers. For each residue, each side-chain dihedral angle is rotated in 10° increments, and the electron density value calculated using a cubic spline interpolation is tabulated at the position of the rotated atom. In sp^3 geometry, for example, the sampled position is 1.53 Å away and oriented 111.1° from the preceding side-chain carbon atom. In regions of electron density that are not occupied by modelled atoms, Ringer peaks $>0.3\sigma$ are significantly enriched at rotameric positions, and χ_1 peaks are strongly correlated with rotameric χ_2 peaks in long side chains, providing evidence that these features correspond to alternative conformers¹³. The contour level of 0.3σ provides an initial working cut-off to detect alternative rotamers in high-resolution electron density maps. Alternative conformers are modelled after inspection of the electron density maps for continuous or correlated electron density for the side chain and subsequently refined.

Comparison of crystal structures. Forty-eight CYPA structures with 100% sequence identity (Supplementary Fig. 1) were superimposed using Theseus⁴¹ and analysed for backbone root-mean-square-deviation (r.m.s.d.) to establish regions of conformational heterogeneity or flexibility.

NMR methods. Unless otherwise specified, NMR samples consisted of 1 mM wild-type or mutant CYPA in 50 mM Na₂HPO₄ pH 6.5, 0.02% NaN₃, 1 mM DTT, 10% D₂O. Constant-time relaxation dispersion spectra^{17,42} were collected in an interleaved manner, processed using NMRPipe⁴³ software, and analysed using NMRView⁴⁴ and custom scripts. Errors in peak intensities were estimated using the variance for non-exchanging peaks, signal to noise, and duplicate points. Errors for the fits were estimated using 200 Monte Carlo simulations. CPMG relaxation dispersion data collected at 25 °C at 500, 600 and 800 MHz not only constrained the fitted parameters but also provided α values for all residues¹⁸.

We note that in the slow exchange regime of Ser99Thr, CPMG relaxation data and fitting them to the Carver–Richards equation is not robust to determine chemical shift differences or populations. The absence of the minor peak, in light of the estimated line-broadening, suggests an upper population limit for this species of about 10%. However, k_1 is well determined in the slow time regime by the value of R_{ex} .

Chemical shift differences between mutant and wild-type backbone amides or side-chain indoles (Trp 121) were considered significant when $\Delta\delta$ was greater than 0.05 p.p.m. in the ¹H dimension or 0.25 p.p.m. in the ¹⁵N dimension. Three-bond J couplings were assessed using difference spectra³⁰.

NOESY experiments were performed at 6 °C in a buffer containing 860 μM AAPF and 100% D₂O using a standard gradient-filtered experiment⁴⁵. Intensity curves were fitted to previously described equations²⁰ in Origin 6.0 using populations for the *cis* and *trans* isomer determined from the intensities of the peaks in a NOESY spectrum with a mixing time of zero. The fits of the data for all three enzyme forms yielded the corresponding exchange rates (k_{ex}), but the same R_1 values for the auto-peaks within experimental error. The bidirectional $k_{\text{cat}}^{\text{isom}}$ was calculated from this k_{ex} using the following equations:

$$k_{\text{ex}} = \frac{v^{\text{isom}}}{[S]}$$

$$v^{\text{isom}} = \frac{k_{\text{cat}}^{\text{isom}} [E][S]}{K_M + [S]}$$

where v^{isom} is the reaction velocity, K_M is the Michaelis-Menten constant, and [S] and [E] are substrate and enzyme concentrations, respectively. For fast dissociation relative to the rate of the isomerization, $K_M \approx K_D$, so:

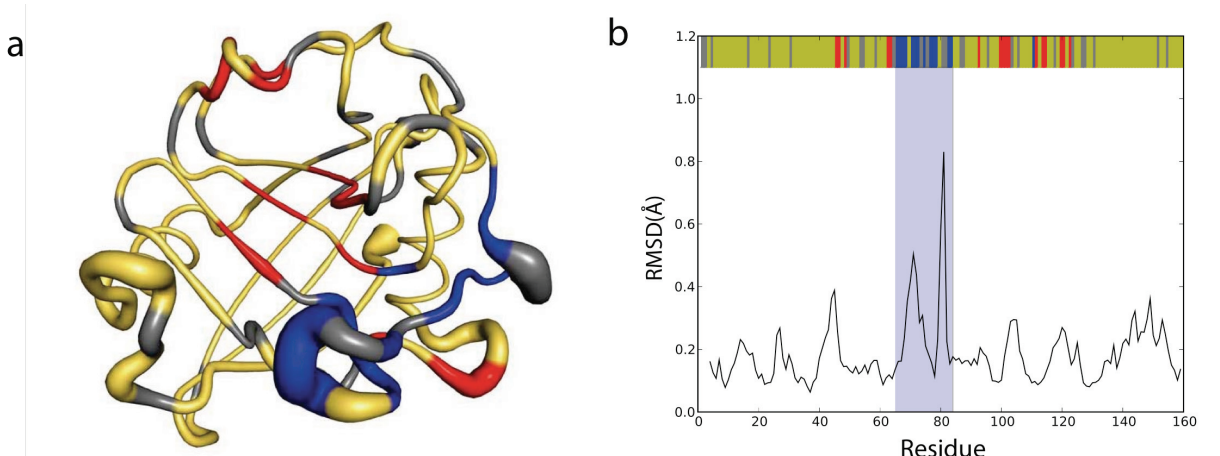
$$k_{\text{cat}}^{\text{isom}} = \frac{k_{\text{ex}}(K_D + [S])}{[E]}$$

This yields a bidirectional $k_{\text{cat}}^{\text{isom}}$ when one uses the K_D averaged for the *cis* and *trans* isomers obtained from the titration experiments.

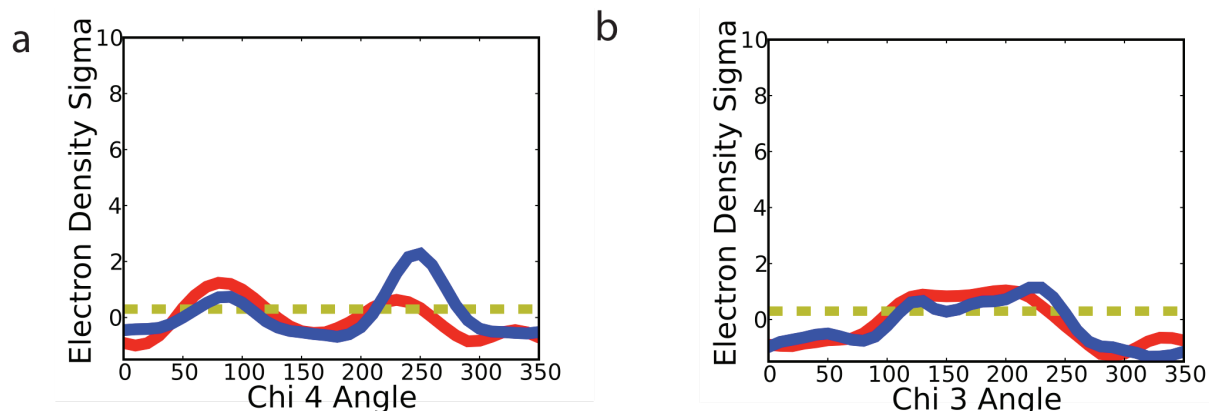
Coupled enzymatic assay. k_{cat}/K_M for the enzyme catalysed *cis*-to-*trans* isomerization of AAPF was measured at 10 °C using the standard protease coupled assay¹⁹.

31. Southworth-Davies, R. J., Medina, M. A., Carmichael, I. & Garman, E. F. Observation of decreased radiation damage at higher dose rates in room temperature protein crystallography. *Structure* 15, 1531–1541 (2007).
32. Otwinowski, Z. & Minor, W. in *Macromolecular Crystallography Part A*, 307–326 (Methods in Enzymology, Vol. 276, Academic, 1997).
33. McCoy, A. J. et al. Phaser crystallographic software. *J. Appl. Crystallogr.* 40, 658–674 (2007).
34. Adams, P. D. et al. PHENIX: building new software for automated crystallographic structure determination. *Acta Crystallogr. D* 58, 1948–1954 (2002).
35. Holton, J. & Alber, T. Automated protein crystal structure determination using ELVES. *Proc. Natl Acad. Sci. USA* 101, 1537–1542 (2004).
36. Kabsch, W. Automatic processing of rotation diffraction data from crystals of initially unknown symmetry and cell constants. *J. Appl. Crystallogr.* 26, 795–800 (1993).
37. Emsley, P. & Cowtan, K. Coot: model-building tools for molecular graphics. *Acta Crystallogr. D* 60, 2126–2132 (2004).
38. Davis, I. W. et al. MolProbity: all-atom contacts and structure validation for proteins and nucleic acids. *Nucleic Acids Res.* 35, W375–W383 (2007).
39. Laskowski, R. A., MacArthur, M. W., Moss, D. S. & Thornton, J. M. Procheck—a program to check the stereochemical quality of protein structures. *J. Appl. Crystallogr.* 26, 283–291 (1993).
40. Delano, W. L. The PyMOL Molecular Graphics System (DeLano Scientific, Palo Alto, 2008); (<http://www.pymol.org>).
41. Theobald, D. L. & Wuttke, D. S. THESEUS: maximum likelihood superpositioning and analysis of macromolecular structures. *Bioinformatics* 22, 2171–2172 (2006).
42. Mulder, F. A. A., Mittermaier, A., Hon, B., Dahlquist, F. W. & Kay, L. E. Studying excited states of proteins by NMR spectroscopy. *Nature Struct. Biol.* 8, 932–935 (2001).
43. Delaglio, F. et al. NMRPipe—a multidimensional spectral processing system based on UNIX pipes. *J. Biomol. NMR* 6, 277–293 (1995).
44. Johnson, B. A. & Blevis, R. A. NMR View—a computer program for the visualization and analysis of NMR data. *J. Biomol. NMR* 4, 603–614 (1994).
45. Jeener, J., Meier, B. H., Bachmann, P. & Ernst, R. R. Investigation of exchange processes by 2-dimensional NMR-spectroscopy. *J. Chem. Phys.* 71, 4546–4553 (1979).

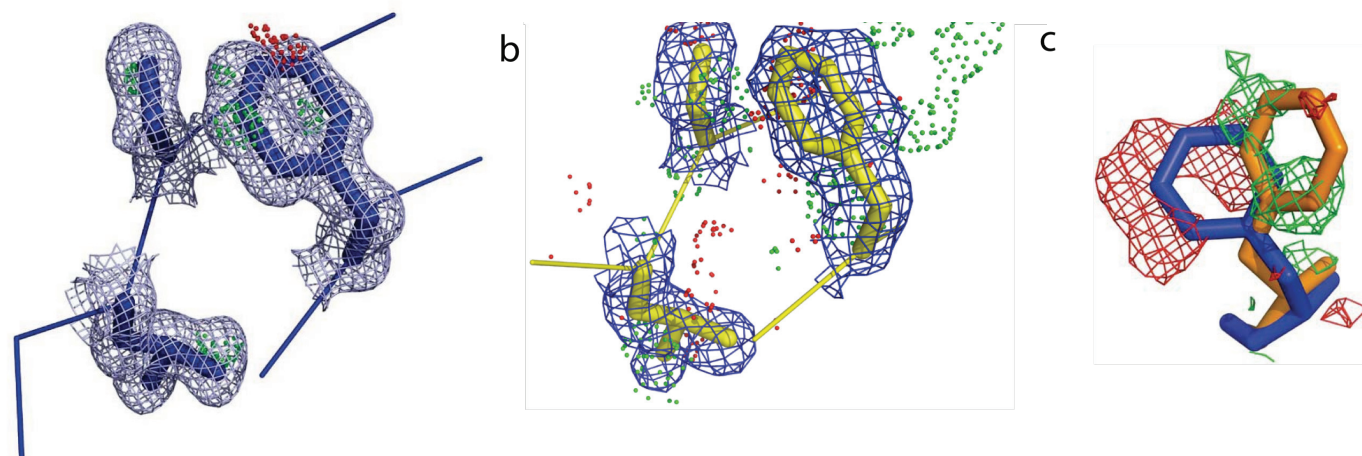
SUPPLEMENTARY INFORMATION



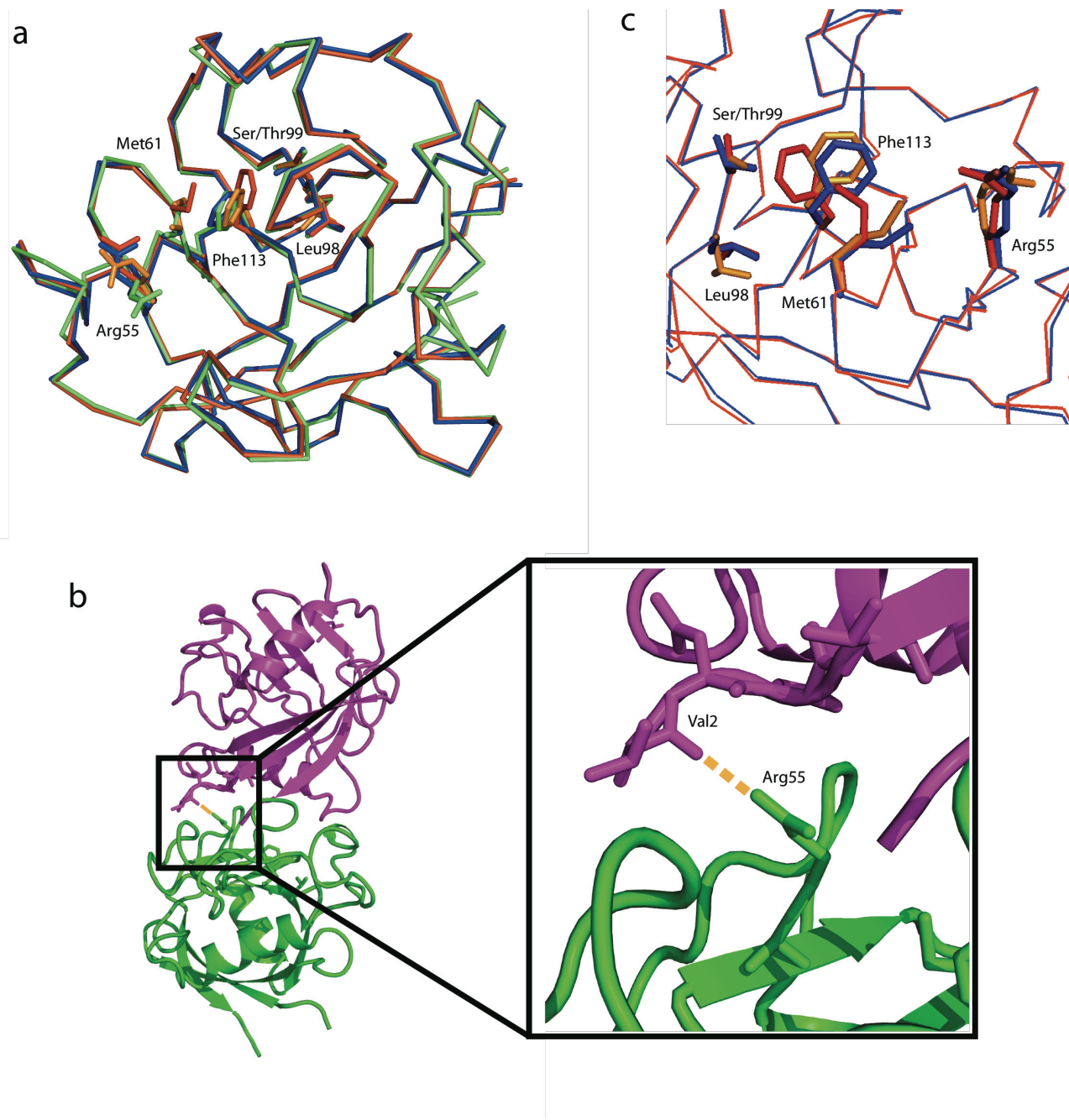
Supplementary Figure 1. Crystal structures of CypA differ in loops but not in residues coupled to the active site. Backbone RMSD from a structural superposition of 48 CypA crystal structures in **a**, sausage representation of with thickness is proportional to backbone RMSD and **b**, as a function of residue number. The color-coding used is based on previous NMR relaxation dispersion experiments (ref. 4): group I (red), group II (blue), residues that do not display R_{EX} (yellow), and prolines or unresolved amides (grey). Backbone differences of group II residues, but not group I residues, explain the different chemical environments of the major and minor states inferred through relaxation dispersion NMR. Forty-eight CypA structures, some of the free enzyme and some with ligands bound, were superimposed using Theseus⁴¹: (Structure_chain)--1ak4_A, 1cwc_A, 1m63_C, 1oca_A, 2cpl_A, 1awq_A, 1cwf_A, 1m9c_A, 1rmh_A, 2cyh_A, 1awr_A, 1cwh_A, 1m9d_A, 1vbs_A, 2rma_A, 1aws_A, 1cwi_A, 1m9e_A, 1vbt_A, 2rmb_A, 1awt_A, 1cwj_A, 1m9f_A, 1w8l_A, 3cyh_A, 1awu_A, 1cwk_A, 1m9x_A, 1w8m_A, 3cys_A, 1awv_A, 1cwl_A, 1m9y_A, 1w8v_A, 4cyh_A, 1bck_A, 1cwm_A, 1mf8_C, 1ynd_A, 5cyh_A, 1cwa_A, 1cwo_A, 1mik_A, 1zkf_A, 1cwb_A, 1fgl_A, 1nmk_A, 2alf_A.



Supplementary Figure 2. Ringer identifies discrete side-chain heterogeneity for active-site residues in the cryogenic (100 K), 1.2-Å-resolution electron density of wild-type CypA. a, Arg55 χ_4 and b, Met61 χ_3 . At room temperature, additional peaks for these and neighboring residues were present in the electron density from data collected at both cryogenic (blue) and room temperature (red) (see also Fig. 1). These data reinforce the point that some CypA residues are polymorphic at both room and cryogenic and others are only polymorphic at room temperature.

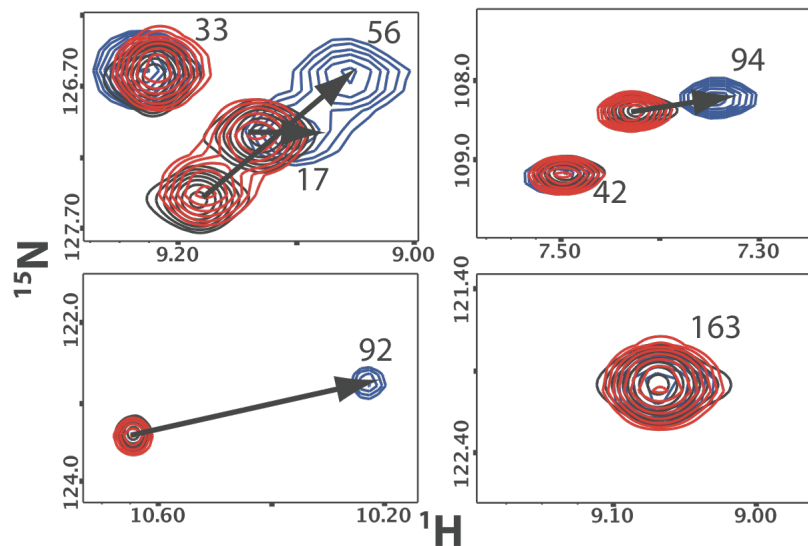


Supplementary Figure 3. The alternate CypA conformations are present at room temperature, but not cryogenic temperatures. **a,** Electron-density maps calculated using X-ray data collected at 100 K define unique conformers of Leu98, Ser99 and Phe113. 2Fo-Fc electron density (blue mesh; 1 σ); positive (green) and negative (red) Fo-Fc difference density (3 σ). The lack of difference density surrounding Phe113, in contrast to the room temperature data shown in Figure 1b, suggests a unique conformation best fits the electron density. 2Fo-Fc electron density around the main chain and the surrounding residues was omitted for clarity. **b,** The alternate conformation is unaffected by the cryoprotectant, 15% xylitol. 2Fo-Fc electron density (blue mesh; 1 σ); positive (green) and negative (red) Fo-Fc difference density (3 σ) calculated from a 1.45-Å-resolution data set collected at room temperature with 15% xylitol present. The difference density pattern is similar to the high-resolution room temperature electron density shown in Figure 1b obtained in the absence of xylitol. **c,** An isomorphous difference map ($F_{\text{room_temperature}} - F_{\text{cryogenic}}$) and phases from the model using the data obtained at 100 K reveals directly the shift to the minor state at room temperature. Negative difference density (red, 2.5 σ) surrounds the major conformation and positive difference density (green, 2.5 σ) reveals the hidden minor state.

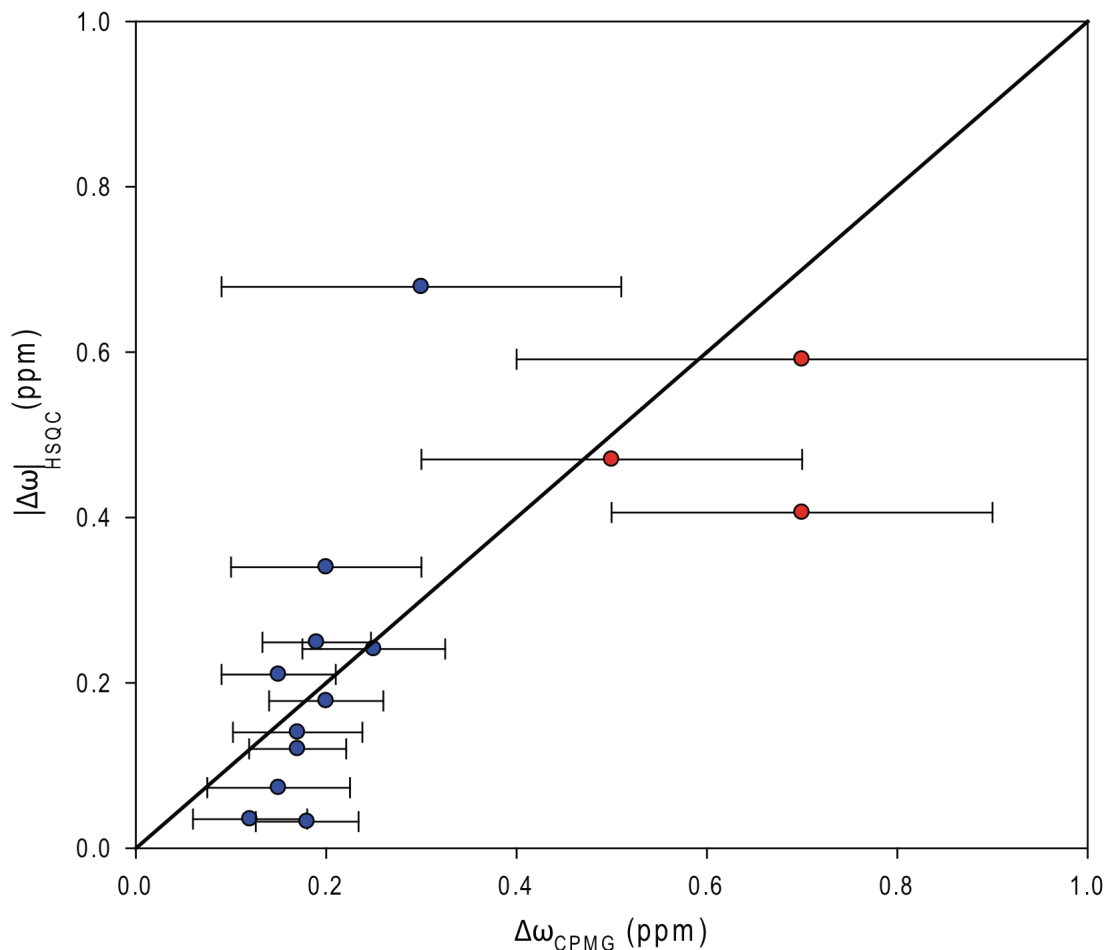


Supplementary Figure 4. The structure of Ser99Thr CypA contains features of the minor conformation of wild-type enzyme. **a**, Ribbon overlay of the structures of wild-type CypA in the orthorhombic crystal form (backbone in orange-red, major-state side chains in red, minor-state side chains in orange), the Ser99Thr mutant trigonal form (green), and Ser99Thr mutant orthorhombic form (blue) with the side-chains Arg55,

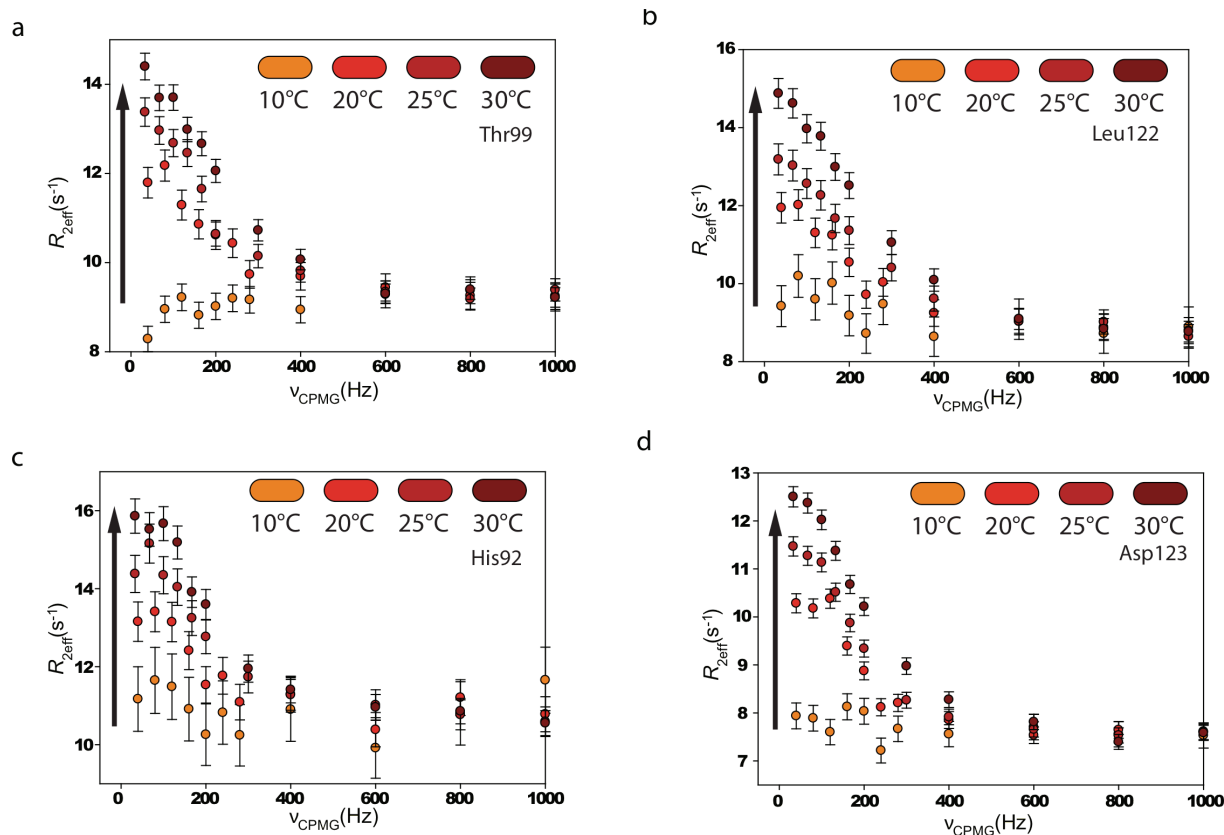
Met61, Leu98, Ser/Thr99 and Phe113 shown in sticks. **b**, Arg55 adopts a different rotamer in the trigonal crystals due to crystal contacts. The Arg55 guanidino group is 3.1 Å (orange line) from the carbonyl oxygen of Val2 of the symmetry-related molecule (magenta). **c**, In the isomorphous orthorhombic crystal forms, Arg55, Phe113 and Thr99 (Ser99 in the wild-type enzyme) adopt similar conformations in the Ser99Thr mutant (blue) and the minor conformational substate of wild-type CypA (orange).



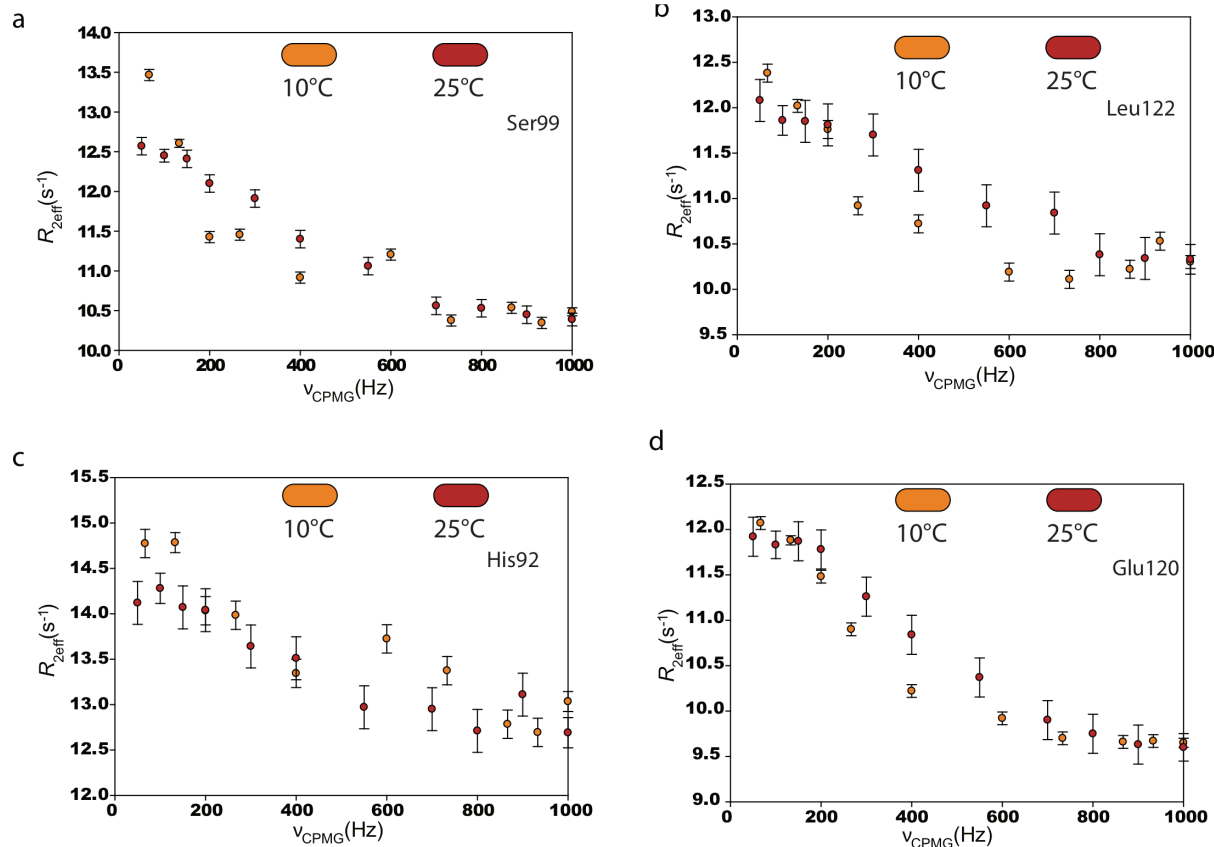
Supplementary Figure 5. Additional residues show that the Ser99Thr mutation shifts the equilibrium toward the minor wild-type conformation. Linear amide chemical shift changes (arrows) between wild-type (black), Lys82Ala (red) and Ser99Thr (blue) CypA reflect the inversion of the major/minor equilibrium due to the Ser99Thr mutation. Residue 163 is shown as a representative residue that does not differ in chemical shift between the major and minor state.



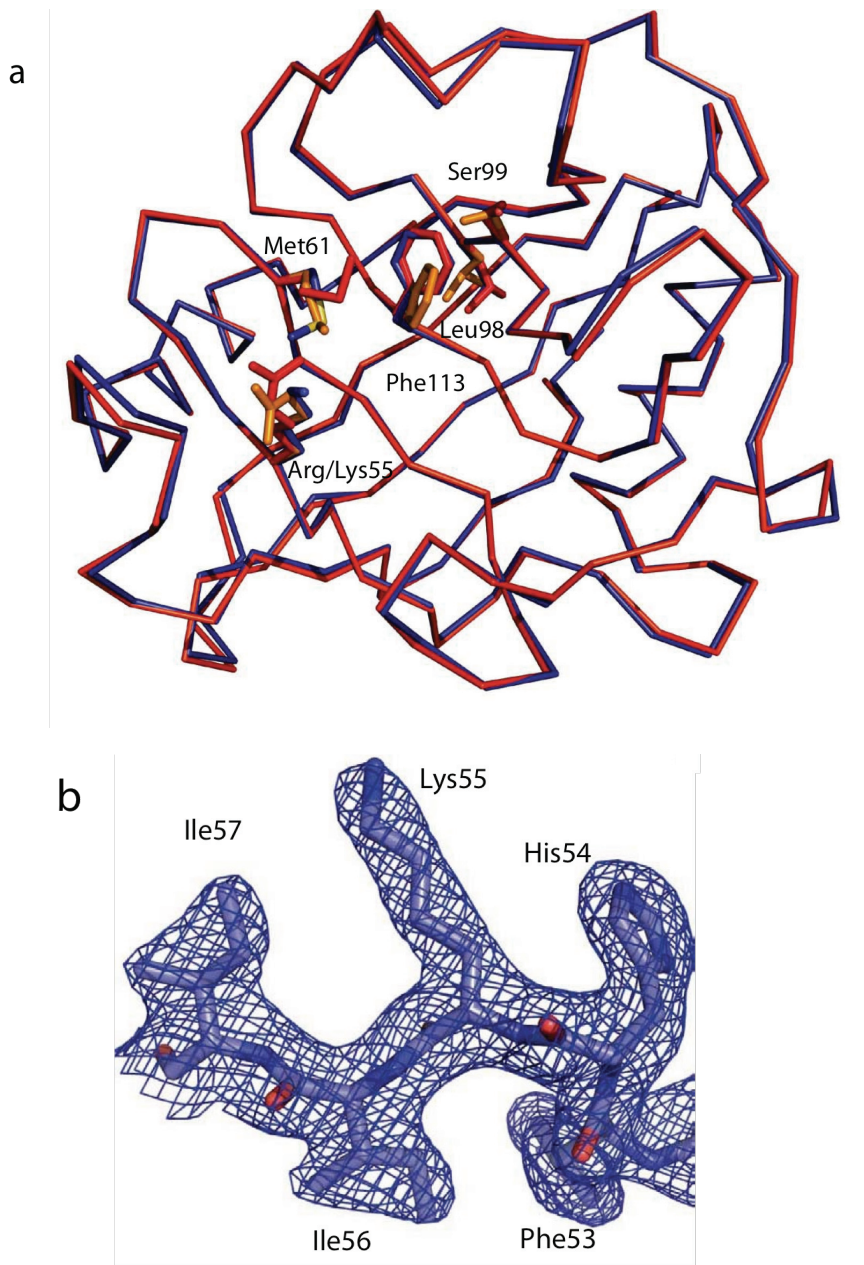
Supplementary Figure 6. Evidence for inversion of minor/major equilibrium in Ser99Thr CypA relative to wild-type CypA. Correlation of ^{13}C methyl (blue) and ^{15}N backbone (red) chemical shift differences between Ser99Thr and wild-type CypA, measured from HSQC spectra, and the chemical shift differences calculated from the corresponding wildtype CPMG relaxation dispersion data fitted to the full Carver Richards equation at 10 °C⁴. The CPMG data⁴ were fit using an improved fitting protocol (see methods). The large percentage uncertainties originate in the very small amplitudes of dispersion (between 0.5 and 1.5 Hz).



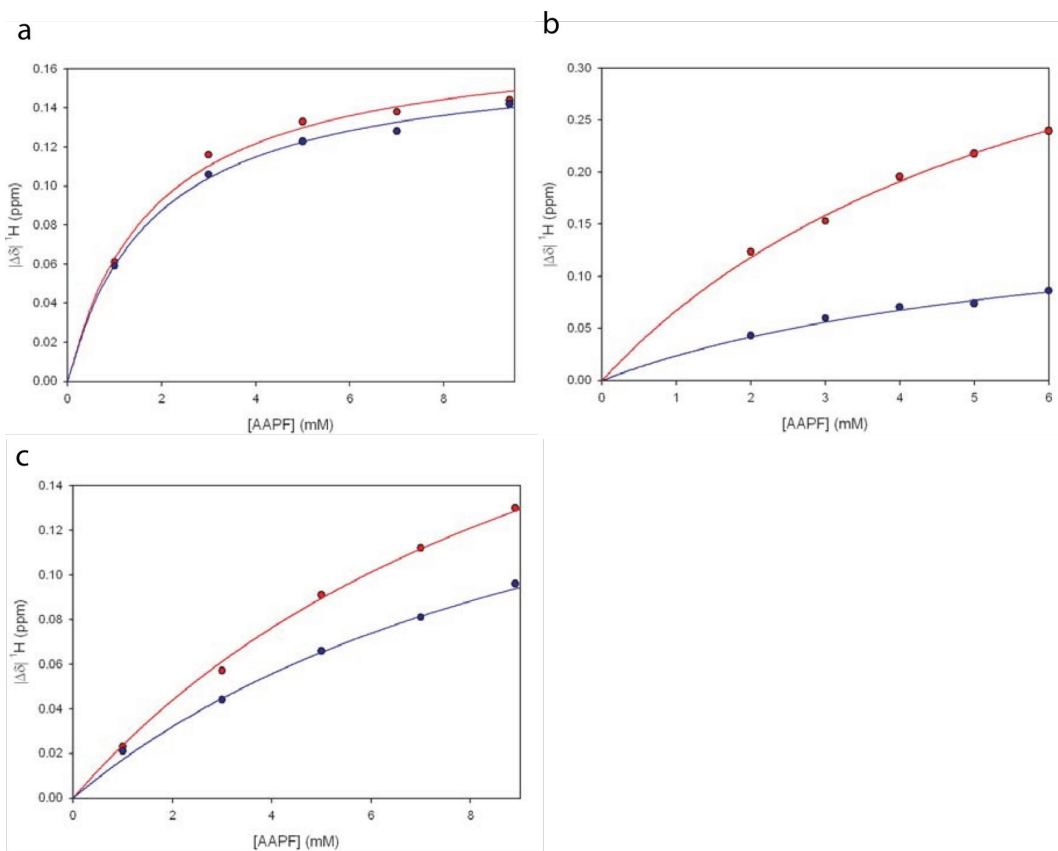
Supplementary Figure 7. Group I residues in the Ser99Thr mutant undergo dynamics in the slow NMR time regime. Temperature dependence of CPMG ^{15}N NMR relaxation data for group I residues, which couple to the active site: **a**, Thr99, **b**, Leu122, **c**, His92, and **d**, Asp123 in Ser99Thr CypA. The Ser99Thr mutation impedes group I conformational dynamics, shifting the motions collectively into the slow NMR time regime. The characteristic increase of R_{EX} with temperature (arrows) demonstrates that $R_{\text{EX}} \sim k_1$, the rate constant for the efflux from the major state. Curves were normalized as in Fig. 3d.



Supplementary Figure 8. Group I residues in wild-type CypA undergo dynamics in the intermediate to fast NMR time regime. Temperature dependence of CPMG ^{15}N NMR relaxation data for group I residues **a**, Ser99, **b**, Leu122, **c**, His92 and **d**, Glu120 in wild-type CypA do not reveal the temperature dependence of group I conformational dynamics as seen in Ser99Thr CypA, revealing that motions occur in the intermediate/fast NMR time regime. Curves were normalized as in Fig. 3d.

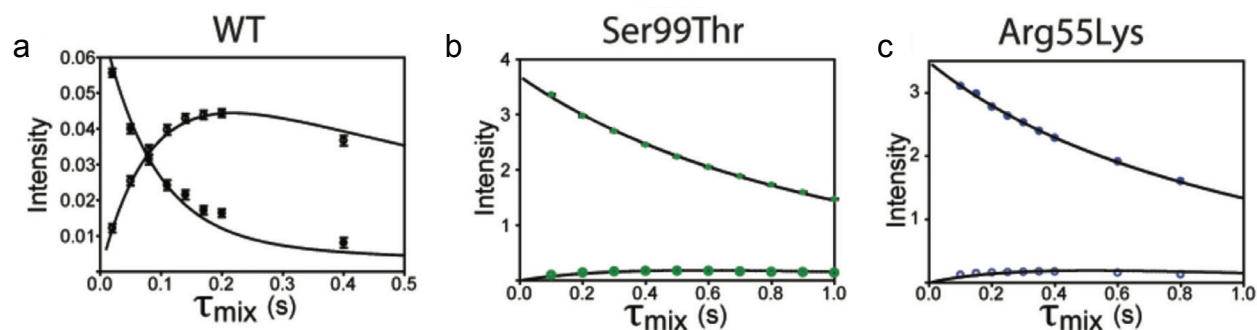


Supplementary Figure 9. X-ray structure of the chemically impeded Arg55Lys mutant. **a**, Arg55Lys CypA (blue) adopts a global structure similar to the wild-type enzyme (backbone in orange-red, major state side chains in red, minor state side chains in orange). **b**, 2Fo-Fc electron density (1σ , 2.4 Å resolution, 100 K data collection temperature) for Lys55 and the neighboring residues. This resolution is not sufficient to monitor alternate conformations by Ringer.



Supplementary Figure 10. NMR measurements of the affinity of CypA variants for the substrate peptide, N-succinyl-Ala-Ala-Pro-Phe-p-nitroanilide (AAPF).

Representative chemical-shift changes for AAPF binding to **a**, wild-type, **b**, Ser99Thr, and **c**, Arg55Lys CypA derived from ^1H - ^{15}N HSQC spectra collected at 6 °C. Changes in proton chemical shift (circles) as a function of peptide concentration were fit for single-site binding (lines). Residues 63 (a, red) and 100 (a, blue), 52 (b, red) and 81 (b, blue), and 101 (c, red) and 102 (c, blue) were among those used in global fits of KD for each variant. The set of residues used to determine the KD's differed for each CypA variant due to changes in resonance overlap. The fitted values are observed KD's (see supplementary table 4) representing population-averaged values for the cis- and trans-isomers.



Supplementary Figure 11. Quantification of catalytic activity of wild-type, Ser99Thr and Arg55Lys mutant forms of CypA. Decay and buildup curves from ^1H - ^1H NOE-exchange spectra collected with different mixing times²¹ of the *cis*-auto peak of Ala2 and the corresponding exchange peak in the presence of **a**, 2.2 μM wild-type or the *trans*-auto peak of Pro3 and the corresponding exchange peak in the presence of **b**, 92 μM Ser99Thr and **c**, Arg55Lys.

Supplementary Table 1. Data collection and refinement statistics.

	WT-Cryo	WT-Room	S99T-Room	S99T-trigonal-cryo	S99T-orthorombic-cryo	R55K-cryo
Space Group	P2 ₁ 2 ₁ 2 ₁	P2 ₁ 2 ₁ 2 ₁	P3 ₂ 1	P3 ₂ 1	P2 ₁ 2 ₁ 2 ₁	P3 ₂ 1
Cell Dimensions a, b, c (Å)	42.4, 51.7, 88.6	43.1, 52.6, 89.3	60.4, 60.4, 95.5	59.7, 59.7, 94.3	42.5, 52.1, 89.1	64.2, 64.2, 93.6
Resolution (Å)	50-1.25 (1.29-1.25)	50-1.39 (1.44-1.39)	50-1.55 (1.61-1.55)	50-1.65 (1.71-1.65)	50-2.31 (2.39-2.31)	50-2.42 (2.51-2.42)
R _{sym}	0.042 (0.564)	0.049 (0.525)	0.102 (0.441)	0.077 (0.410)	0.092 (0.193)	0.131 (0.572)
I/σ	38.3 (3.6)	33.8 (1.9)	21.0 (3.0)	24.8 (2.9)	11.8 (3.7)	16.4 (3.9)
Completeness (%)	99.7 (99.1)	99.2 (92.3)	90.8 (55.0)	99.2 (92.1)	87.3 (48.4)	100 (100)
Redundancy	7.4 (7.1)	7.4 (2.9)	13.3 (5.6)	7.4 (4.2)	3.3 (1.9)	9.8 (9.3)
Reflections	54749 (5385)	41145 (3767)	27237 (1609)	23875 (2180)	7936 (430)	8900 (853)
R _{work} /R _{free} (%)	12.9/14.9	12.2/16.0	10.7/14.8	14.7/17.6	17.6/24.7	17.7/23.6
No. atoms						
• Protein	2740	3040	2447	2447	2482	2477
• Water	269	132	119	218	95	59
Average B-factors						
• Protein (Å ²)	13.66	23.68	20.14	15.24	27.61	33.96
• Water (Å ²)	28.91	37.28	33.34	29.79	32.15	34.83
R.M.S deviations						
• Angles (°)	1.307	1.264	1.310	1.445	1.569	1.762
• Bonds (Å)	0.010	0.011	0.011	0.014	0.016	0.019
Beamline	SSRL 9-1	ALS 12.3.1	ALS 12.3.1	ALS 8.3.1	ALS 8.3.1	ALS 8.3.1
Data collection temperature	100K	288K	288K	100K	100K	100K
PDB code	3K0M	3K0N	3K0O	3K0P	3K0Q	3K0R

The highest resolution shell is shown in parentheses.

Supplementary Table 2: Aromatic 3-bond J (3J) couplings in CypA

Residue	WT		Ser99Thr	
	$^3J_{C' C_\gamma}$ (Hz)	$^3J_{NC_\gamma}$ (Hz)	$^3J_{C' C_\gamma}$ (Hz)	$^3J_{NC_\gamma}$ (Hz)
Phe25	3.62 ± 0.11	0.78 ± 0.29	3.75 ± 0.09	0.75 ± 0.27
Tyr79	3.31 ± 0.12	1.01 ± 0.32	3.39 ± 0.08	0.67 ± 0.34
Phe88	3.64 ± 0.14	0.77 ± 0.31	3.28 ± 0.16	0.54 ± 0.36
His92	3.64 ± 0.18	0.97 ± 0.36	3.91 ± 0.17	1.23 ± 0.33
Phe113	1.12 ± 0.63	0.91 ± 0.32	2.77 ± 0.23	0.81 ± 0.41
Phe145	3.35 ± 0.12	0.89 ± 0.24	3.49 ± 0.09	0.25 ± 0.76

3J couplings between backbone atoms and $C\gamma^{29}$, showing a change in Phe113 rotameric state (highlighted in bold) between WT and Ser99Thr. Only residues with full data for both variants are shown. All experiments were performed at 25 °C, except WT Phe113 $^3J_{C' C_\gamma}$, taken at 5 °C due to resonance overlap.

Supplementary Table 3: Relaxation dispersion parameters for Ser99Thr CypA

Residue	$10^{\circ}\text{C } R_{\text{EX}} (\text{/s})^{\text{a}}$	$20^{\circ}\text{C } R_{\text{EX}} (\text{/s})^{\text{a}}$	$25^{\circ}\text{C } R_{\text{EX}} (\text{/s})^{\text{a}}$	$30^{\circ}\text{C } R_{\text{EX}} (\text{/s})^{\text{a}}$	$\alpha (25^{\circ}\text{C})^{\text{b}}$
90	1.7 ± 0.9	2.2 ± 0.4	2.1 ± 0.4	2.1 ± 0.3	0.3
92	0.8 ± 1.1	2.9 ± 0.7	4.1 ± 0.6	5.2 ± 0.5	0.0
99	N/D ^c	3.2 ± 0.5	4.3 ± 0.4	5.5 ± 0.4	0.0
113	1.1 ± 0.7	2.8 ± 0.5	3.9 ± 0.4	3.6 ± 0.4	0.1
114	1.4 ± 0.7	2.2 ± 0.5	2.0 ± 0.4	N/D ^c	0.5
119	0.8 ± 0.3	2.9 ± 0.2	3.3 ± 0.2	2.8 ± 0.2	0.9
120	0.9 ± 0.4	3.3 ± 0.5	4.6 ± 0.3	5.7 ± 0.4	0.3
122	0.6 ± 0.7	3.4 ± 0.3	4.7 ± 0.5	6.4 ± 0.5	0.0
123	0.6 ± 0.4	3.1 ± 0.5	4.3 ± 0.3	5.4 ± 0.3	0.0
126	N/D ^c	3.8 ± 0.5	4.0 ± 0.4	4.4 ± 0.4	0.2
127	0.8 ± 0.4	3.2 ± 0.9	5.5 ± 1.0	6.9 ± 1.1	0.0
128	1.5 ± 2.0	2.1 ± 1.1	5.1 ± 1.1	7.6 ± 1.2	0.0
$k_1 (R_{\text{EX}})^{\text{d}}$	1.0 ± 0.4	2.9 ± 0.5	4.0 ± 1.1	4.7 ± 2.0	
$k_1 (\text{fit})^{\text{e}}$	1.00 ± 0.20	2.96 ± 0.18	4.98 ± 0.65	8.22 ± 0.49	

Relaxation parameters for group I residues in Ser99Thr CypA that were used in global fitting. ^a apparent R_{EX} estimated from relaxation-dispersion curves at 600 MHz. ^b α^{19} calculated from apparent R_{EX} at 800, 600, and 500 MHz. ^c Not determined due to resonance overlap or excessive noise. ^d k_1 calculated as average of apparent R_{EX} of all group I residues. ^e k_1 fitted globally from group I relaxation-dispersion data using the full Carver-Richards equation. It is apparent that above 25°C, the exchange moves form the slow NMR time regime to the intermediate NMR time regime.

Supplementary Table 4. Kinetic constants for the reaction of CypA variants with the substrate N-succinyl-Ala-Ala-Pro-Phe-p-nitroanilide (AAPF).

	k_{cat}/K_M ($s^{-1}M^{-1}$) ^a	K_D (mM) ^b	k_{cat}^{isom} (s^{-1}) ^c
WT	$1.4 \times 10^7 \pm 0.1 \times 10^7$	1.8 ± 0.14	$1.3 \times 10^4 \pm 800$
Ser99Thr	$4.5 \times 10^4 \pm 0.4 \times 10^4$	6.7 ± 0.8	$1.9 \times 10^2 \pm 20$
Arg55Lys	$1.4 \times 10^4 \pm 0.2 \times 10^4$	11.3 ± 2.5	$3.8 \times 10^2 \pm 90$

(mean +/- s.d.)

^a k_{cat}/K_M for the cis to trans direction determined from the coupled chymotrypsin assay²⁰ at 10°C. ^b determined from NMR titration data at 6°C. ^c determined from the NOESY exchange spectra at 6°C using the K_D from^b.